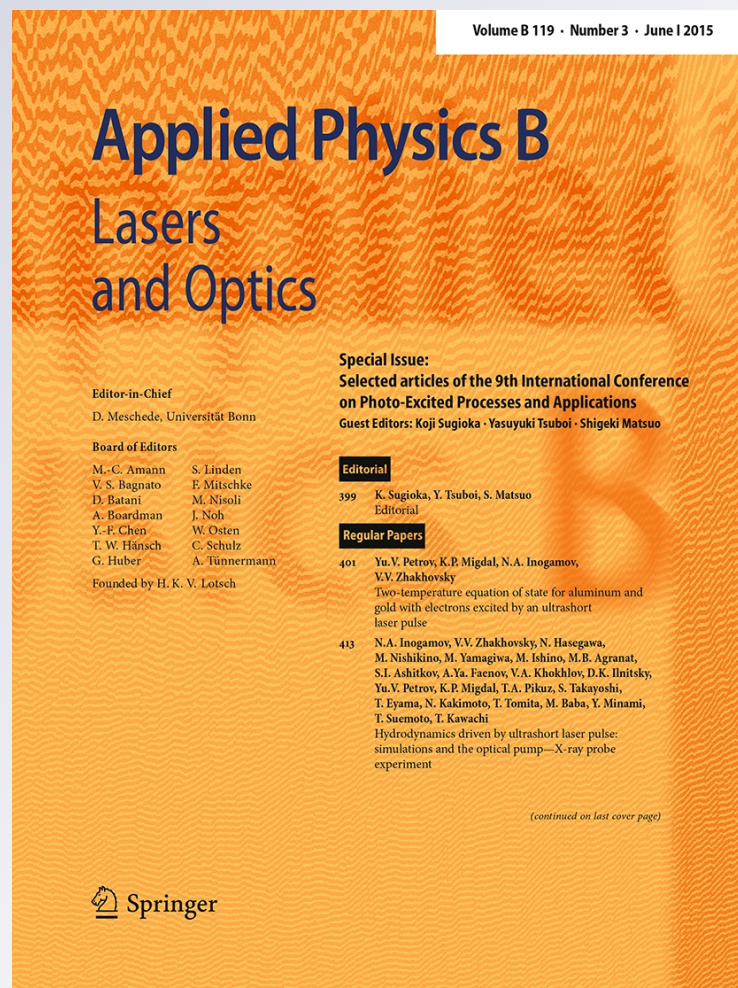# Two-temperature equation of state for aluminum and gold with electrons excited by an ultrashort laser pulse

Yu. V. Petrov, K. P. Migdal, N. A. Inogamov & V. V. Zhakhovsky

Springer

Springer

CrossMark

Two-temperature equation of state for aluminum and gold with electrons excited by an ultrashort laser pulse

Yu. V. Petrov · K. P. Migdal · N. A. Inogamov · V. V. Zhakhovsky

Abstract A short laser pulse converts metal into a two-temperature state with the electron temperature higher than the ion temperature. To describe the electron contributions to the total internal energy and pressure arising as a result of electron heating, we develop the new analytic approximation formulae for two-temperature thermodynamics of metal. Those approximations are based on quantum calculations performed with density functional theory (DFT) packages. DFT calculations provide the internal energies and pressures for densities of the order of solid-state density and for electron temperatures up to 55 kK. The new analytic approximations give a better accuracy in hydrodynamic simulation of laser–matter interaction and should be used instead of the less accurate expressions based on the Fermi model of ideal electron gas, which is widely used for two-temperature states of metal.

Y. V. Petrov · N. A. Inogamov
Landau Institute for Theoretical Physics of Russian Academy of Sciences, 142432 Chernogolovka, Russian Federation

Y. V. Petrov
Moscow Institute of Physics and Technology (State University), 141700 Dolgoprudny, Russian Federation

K. P. Migdal · N. A. Inogamov (✉) · V. V. Zhakhovsky
All-Russia Research Institute of Automatics (SC Rosatom), 127055 Moscow, Russian Federation
e-mail: nailinogamov@gmail.com

V. V. Zhakhovsky
Joint Institute of High Temperatures of Russian Academy of Sciences, 125412 Moscow, Russian Federation

1 Introduction

Processes involved in the short pulse laser–matter interaction have many important technological applications from production of chips and solar cells to medicine. The predictive calculation methods are strongly required to optimize those advanced technologies. Quantitative description of the corresponding processes is based on two-temperature (2T) hydrodynamic model (2T-HD) [1–5]. 2T-HD equations are

$$\rho(x^0, t)\frac{\partial x(x^0, t)}{\partial x^0} = \rho^0, \tag{1}$$

$$\rho^0 \frac{\partial u}{\partial t} = -\frac{\partial P(x^0, t)}{\partial x^0}, \tag{2}$$

$$\frac{\partial x(x^0, t)}{\partial t} = u(x^0, t), \tag{3}$$

$$\rho^0 \frac{\partial (E_e/\rho)}{\partial t} = -\frac{\partial q}{\partial x^0} - \dot{E}_{ei} + \frac{\rho^0}{\rho} Q - P_e \frac{\partial u}{\partial x^0}, \tag{4}$$

$$\dot{E}_{ei} = \frac{\rho^0}{\rho} \alpha \cdot (T_e - T_i), \qquad q = -\frac{\rho \kappa}{\rho^0} \frac{\partial T_e}{\partial x^0}, \tag{5}$$

$$\rho^0 \frac{\partial (E_i/\rho)}{\partial t} = \dot{E}_{ei} - P_i \frac{\partial u}{\partial x^0}, \tag{6}$$

$$Q = \frac{F_{abs}}{\sqrt{\pi}\, \tau_L\, \delta} \exp\left(-\frac{t^2}{\tau_L^2}\right) \exp\left(-\frac{x}{\delta}\right) \theta(x). \tag{7}$$

Here (1) is a mass conservation equation, $x(x^0, t)$ is a trajectory of Lagrangian particle with the Lagrangian coordinate x^0, $x(x^0, t = -\infty) = x^0$, ρ^0 is an initial density; T_i and

T_e are ion and electron temperatures, respectively; (2) is a momentum equation, $u(x^0, t)$ is a velocity of the Lagrangian particle; (3) is a kinematic condition; (4) is an energy balance for electron subsystem [6, 7]; definitions of the electron–ion energy exchange power and the electron heat conduction flux are given in (5); (6) is an energy balance for the ion subsystem [6, 7]; (7) is a laser power source per unit volume in a skin layer δ, and τ_L is the duration of a pulse. FWHM is $2(\log 2)\tau_L$. Integration starts at the time $t = -5\tau_L$.

To solve those equations, the thermodynamic and kinetic parameters are required. The kinetic parameters are the electron heat conduction coefficient κ and the electron–ion energy exchange coefficient α. The thermodynamic parameters are the total $p = p_e + p_i$ and partial p_e, p_i pressures for electrons and ions, as well as the partial internal energies E_e, E_i and the corresponding heat capacities at constant volume c_e, c_i.

The 2T model is valid if the absorbed fluence F_{abs} is larger than a threshold of few mJ/cm^2. For fluences below this threshold, the electron distribution function cannot be approximated by the Fermi distribution because the electron–electron relaxation time t_{ee} is comparable with the electron–ion relaxation time t_{eq}, where t_{eq} is roughly few picoseconds. Applications of our interest require the absorbed fluences F_{abs} of the order of the melting threshold and higher. The melting threshold is of the order of 20 mJ/cm2 for bulk metal targets. Therefore, the 2T model based on the Fermi distribution is applicable because the hot electrons spread far enough above the Fermi level and the electron–electron relaxation is fast enough as $t_{ee} \ll t_{eq}$.

Here our recent progress in description of thermodynamics of the 2T states of metals calculated by a density functional theory (DFT) method is reported. We consider solely the thermodynamic properties of metals with electron subsystem highly excited by the laser irradiation, so the thermal contribution to the electron internal energy, electron pressure, and the electron Gruneisen parameter is in focus only. Our calculations of the kinetic coefficients of metals in two-temperature states, including the electron heat conductivity and electron–phonon coupling, as functions not only of the electron temperature but the density as well, takes some time to be accomplished.

Section 2 shows the electron spectra and a dependence of the Fermi energy $E_F(\rho)$ from the crystal density ρ. The qualitative differences in thermodynamics between aluminum and gold are demonstrated. Aluminum behaves as a Fermi gas metal, while gold significantly differs from the Fermi model because the functions $E_F(\rho)$ differ, see Fig. 3 below. The low-temperature approximations of internal energy and pressure are given in Sect. 3. It uses results of Sect. 2 concerning the dependence of the Fermi energy $E_F(\rho)$. In Sect. 4, the high-temperature approximation is presented. Transition from the low- to high-temperature
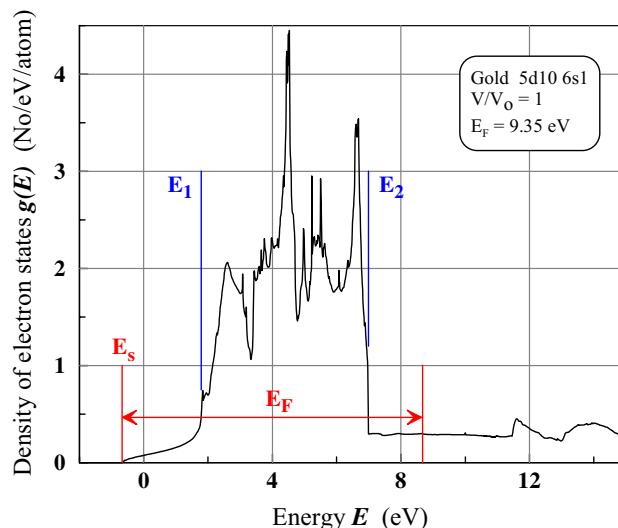

Fig. 1 Conduction band structure of cold gold 5d^{10}6s^1 at $T_i = 0$, $T_e = 0$ and normal density $V/V_0 = 1$. Calculations of spectra and thermodynamics of gold were performed with VASP package, see details in "Appendix 1. " The energy range labeled E_F contains 11 electrons. The Fermi energy E_F is reckoned from the bottom point E_s of s-band. E_1 and E_2 indicate the left and right edge of d-band, respectively
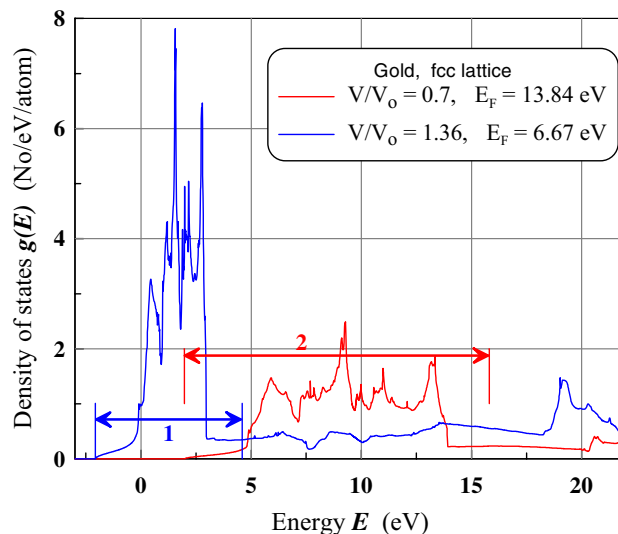

Fig. 2 Expansion of electron spectra with compression ratio V/V_0; markers 1 and 2 show the Fermi energies $E_F(V/V_0)$ for the two different specific volumes

approximations is associated with gradual decrease in the electron degeneracy. In Sect. 4, the final simple analytical approximation formulae for electron energy and pressure are given. They combine together the low- and high-temperature approximations. The ion contribution taken from a wide-range equation of state (EoS) [8, 9] together with the
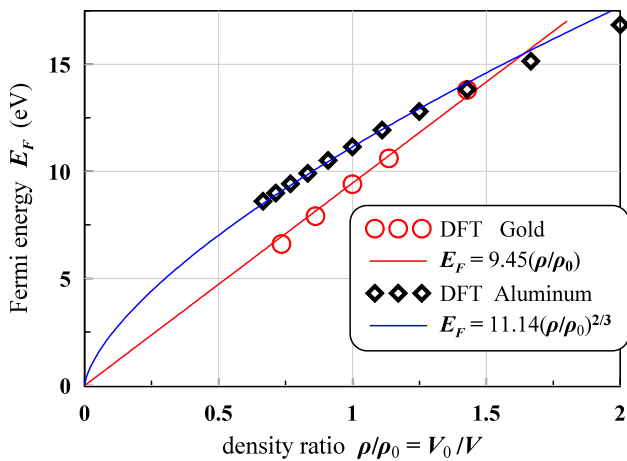
Fig. 3 Expansion of electron spectra with increase of density ratio ρ/ρ_o. Composite results obtained from many spectra as those shown in Fig. 2. Here $E_F \equiv \mu(T_e = 0, \rho)$ is the Fermi energy, $\mu(T_e, \rho)$ is a chemical potential. For Al the packages VASP and Elk both were used, see "Appendix 1 " for calculation details. Since the results for Al obtained by both packages are close to each other, the Elk data are shown only. As was said, the package VASP was employed for gold

calculated electron contribution to thermodynamics provides a final 2T EoS. The procedure of summation of the electron and ion parts is described in [10, 11]. The derived analytical expressions are compared with results of DFT calculations in Sects. 5 and 6.

2 Electron band structure

Electron spectrum obtained with the VASP package is shown in Fig. 1. The calculated spectrum corresponds to fcc lattice of uncompressed gold at the compression ratio $V/V_o = \rho_o/rho = 1$, where ρ_o is a density at the normal conditions. Other details of the VASP calculation are given in "Appendix 1. " The spectrum of gold shown in Fig. 1 agrees with the works [12, 13].

To model the rarefaction and compression waves induced by a fast laser heating during the 2T stage with the usage 2T-HD code (1–7), the effect of mass density variation on hot electron additions to the thermodynamics should be taken into account. Compression/rarefaction is an important factor changing the electron spectra as it can be seen in Figs. 2 and 3. The compression enlarges a band width and decreases the effective electron masses in gold (the mass change with compression is not shown on the Figures). By contrast, our DFT calculations show that the effective mass does not change with compression/rarefaction in the considered range of densities in aluminum.

For aluminum, the Fermi gas model is applicable. The value of chemical potential $\mu(T_e, n)$ in the cold metal with $T_e = 0$ and an ion concentration n is the Fermi energy E_F :

$$E_F(n) \equiv \mu(T_e = 0, n).$$

In the Fermi gas model, the Fermi energy scales with density as [14]

$$E_F = \frac{(3\pi^2)^{2/3}}{2} \frac{\hbar^2}{m_e} n_e^{2/3}, \qquad (8)$$

where n_e is an electron concentration. In Fig. 3, the dependencies of $E_F(n)$ for Au and Al are shown. There is a qualitative difference between these two metals. In aluminum the energy E_F scales as $\approx n^{2/3}$ (8), while in gold the scaling is $\approx n^\beta$, where $\beta \approx 1$. This means that Al can be described well by the Fermi gas model, while for gold, this model is not applicable.

3 Low-temperature thermodynamics

Let us consider the significantly degenerate case of $k_B T_e \ll E_F$. For the Fermi gas the thermal addition per atom E_{low} to the electron energy is given by

$$E_{low}(n, T_e) = z E_F \left[\frac{\pi^2}{4} \left(\frac{k_B T_e}{E_F} \right)^2 - \frac{3\pi^4}{80} \left(\frac{k_B T_e}{E_F} \right)^4 \right]. \quad (9)$$

Equation (9) derived in "Appendix 2 " is written for a single-band metal with a fixed number of electrons z in the band.

For gold the energy E_F scales as $E_F \propto n \propto (n/n_o) = x$, where n_o is a concentration at the normal conditions, see Fig. 3. Therefore we can approximate the (n, T_e) dependence of thermal electron energy in the low-temperature range as

$$E_{low}(n, T_e) = E_F^o \left(e_2 \frac{t^2}{x} + e_4 \frac{t^4}{x^3} \right), \quad t = 2 \frac{k_B T_e}{E_F^o}. \quad (10)$$

In such approximation (10), we neglect the weak dependence of number z on a relative concentration of atoms $x = n/n_o$. The Fermi energy at the normal concentration $n = n_o$

$$E_F^o = E_F(n/n_0 = 1)$$

is taken from DFT data. The e_4 is an adjustable dimensionless coefficient. Below we combine the low- and high-temperature approximations and define the coefficients minimizing the integral of mean-square deviations of our approximation from the (n, T_e)-grid points calculated by the DFT code.

In a single-band Fermi gas with an effective electron mass insensitive to the density variations, the electron thermal addition to the pressure is

$$\frac{p_{low}(n, T_e)}{z n E_F} = \frac{\pi^2}{6} \left(\frac{k_B T_e}{E_F} \right)^2 - \frac{\pi^4}{40} \left(\frac{k_B T_e}{E_F} \right)^4, \quad (11)$$

see "Appendix 2" where this expression is derived. Therefore, we will search for a low-temperature pressure approximation in a form

$$p_{\text{low}}(x, T_e) = p^o \left(p_2 t^2 + p_4 \frac{t^4}{x^2} \right). \tag{12}$$

In Eq. (12), the pressure p^o is $p^o = n_o E_F^o = 88.75$ GPa, $E_F^o = 9.4$ eV, and p_2, p_4 are dimensionless coefficients witch do not depend on either n or T_e.

4 High-temperature thermodynamics and combined approximations

Degeneracy of electrons gradually decreases as the temperature T_e increases. In such condition, the thermal electron energy per atom and thermal electron pressure tend to expressions for the ideal non-degenerate gas $E \sim zT_e$ and $p \sim znT_e$, respectively. We assume that for the energy per atom the high-temperature transition to the non-degenerate case is expressed by

$$\frac{E_{\text{high}}(x, T_e)}{E_F^o e_1 t^{1+\delta_e}} = z_0 + \frac{1 - z_0 - z_2}{x^{m_1}} + \frac{z_2}{x^{m_2}}, \tag{13}$$

where the energy is measured in eV/atom. We assume also that the high-temperature transition for pressure is expressed by

$$\frac{p_{\text{high}}(x, T_e)}{p^o p_1 x t^{1+\delta_p}} = y_0 + (1 - y_0 - y_2)x^{k_1} + y_2 x^{k_2}, \tag{14}$$

where the pressure is measured in GPa.

Approximation formulae combining the low- (10, 12) and high- (13, 14) temperature expressions are

$$E_e(x, T_e) = (E_{\text{low}}^{-1} + E_{\text{high}}^{-1})^{-1}, \tag{15}$$

$$p_e(x, T_e) = (p_{\text{low}}^{-1} + p_{\text{high}}^{-1})^{-1}. \tag{16}$$

We have found the fitting coefficients providing the minimal deviation of the DFT data for E_e and p_e from the expressions (15) and (16). For energy, those coefficients are

$e_2 = 1.13095$, $e_4 = 86.7435$, $e_1 = 2.33349$,
$z_0 = 0.880896$, $z_2 = -0.0364397$,
$m_1 = 4.6121$, $m_2 = 9.75613$, $\delta_e = 0.730093$,
$E_F^o = 9.4$(eV), $t = 2k_B T_e / E_F^o$.

The coefficient e_2 was calculated from the experimental coefficient $\gamma = 67.6$ J / K^2/ m^3, see below.

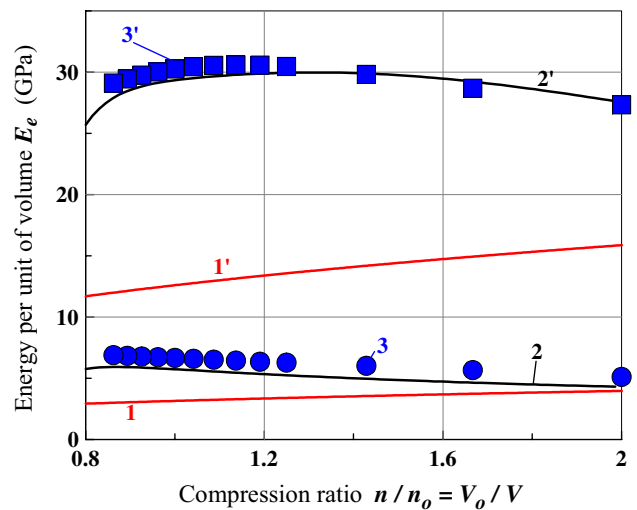For electron pressure, the fitting coefficients are

Fig. 4 The *red curves* 1 and 1' are given by the Fermi gas expression $E_e = \gamma T_e^2/2$ for $T_e = 10$ kK and $T_e = 20$ kK, respectively; the *black curves* 2 and 2' are approximations (15) for $T_e = 10$ kK and $T_e = 20$ kK; the *filled circles* 3 and the *filled squares* 3' are DFT results for $T_e = 10$ kK and $T_e = 20$ kK. The calculated electronic thermal energy of gold strongly deviates from energy derived from the Fermi gas model, even slopes of *black* and *red curves* have opposite signs
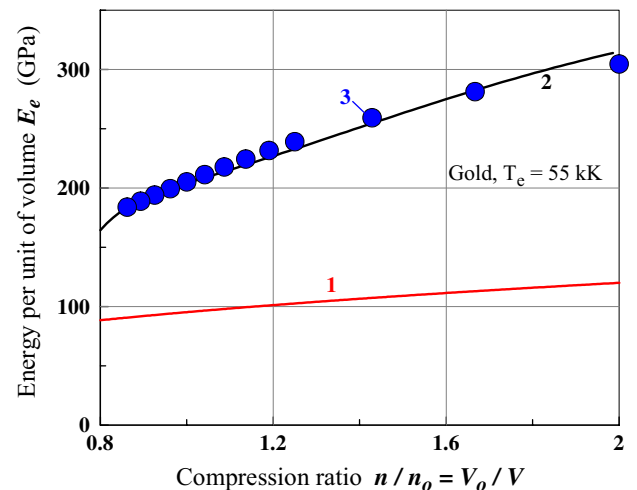

Fig. 5 DFT data (*red curve* 1) with its approximation (*black curve* 2) and the Fermi gas results (*filled circles* 3) for gold at the constant electron temperature $T_e = 55$ kK

$p_2 = 1.3279$, $p_4 = 51.3404$, $p_1 = 1.4515$,
$y_0 = -0.76568$, $y_2 = -0.0274214$,
$k_1 = 0.311491$, $k_2 = 5.1086$, $\delta_p = 0.400865$,
$p_0 = 88.7466$ (GPa), $E_F^o = 9.4$(eV), $t = 2k_B T_e / E_F^o$.

The (ρ, T_e) grid contains $16 \times 16 = 256$ points, where E_e and p_e were calculated with DFT.

5 Comparison with DFT data for energy

DFT calculations were performed for the cold fcc crystal lattice of gold with temperature $T_i = 0$. Density of gold was varied by adjusting the lattice constant [10, 11, 15, 16]. The electron thermal contributions to the energy E_e and pressure p_e were obtained by extracting the cold energy $E(\rho, T_e = 0)$ and pressure $p(\rho, T_e = 0)$ from the total energy $E(\rho, T_e)$ and pressure $p(\rho, T_e)$ of crystal. Values of $E(\rho, T_e)$ and $p(\rho, T_e)$ for the (ρ, T_e)-grid were calculated using the DFT packages, see "Appendix 1".

Figure 4 shows the DFT calculations, their approximation, and the Fermi gas theory results. The Fermi theory data $E_e = \gamma T_e^2 / 2$ are given by the curves 1 and 1', where the coefficient γ is given by

$$\gamma = (\pi/3)^{2/3} k_B^2 / \hbar^2 \, m_e \, n_e^{1/3}. \tag{17}$$

For $z = 1$ and the electron mass m_e equal to the vacuum value, we have $\gamma = 63 \text{ J/K}^2/\text{m}^3$, where the electron concentration is $n_e = zn$. Value $\gamma = 63 \text{ J/ K}^2/\text{ m}^3$ used in Figs. 4 and 5 is close to the experimental low-temperature value $\gamma = 67.6 \text{ J/K}^2/\text{m}^3$ [17, 18].

DFT calculation results for the constant temperatures $T_e = 10$ kK and $T_e = 20$ kK are given by the curves 3 and 3', while the Fermi gas dependencies are shown by the curves 1 and 1' in Fig. 4. The approximation (15) of the DFT results for those temperatures is presented by the curves 2 and 2'. One can see that for the temperatures T_e higher than 10 kK the Fermi gas approach $E_e = \gamma T_e^2 / 2$ significantly underestimates the electron thermal energy in the shown range of crystal densities. This conclusion for normal density gold has been made first in [17]. It is obvious that the accurate approximations required for 2T hydrodynamic modeling should include density dependence because the significant rarefaction and compression take place during 2T stage produced by the short laser pulse heating [19, 20], especially in gold having slow electron–ion temperature relaxation.

It is remarkable that for the temperatures T_e lower than 20 kK the volume density of electron thermal energy E_e slightly *decreases* as a density ratio n/n_o increases at the fixed T_e. While it should increase according to the Fermi gas model (see curves 1 and 1' in Fig. 4) as $E_e = \gamma T_e^2 / 2 \propto m_e z^{1/3} n^{1/3} \propto n^{1/3}$ at a constant electron effective mass m_e and a charge z, and at the fixed temperature T_e. Of course, this follows the same line as behavior of the Fermi energy $E_F(n)$ from density shown in Fig. 3. At higher temperatures T_e the Fermi gas energy $E_e(n, T_e) = \gamma T_e^2 / 2$ is also significantly below the DFT data and cannot be used for accurate hydrodynamic modeling of the laser–matter interaction, see Fig. 5. At this temperature, the DFT slope becomes positive—the energy per unit volume increases with density because the electron subsystem gradually loses its degeneracy.
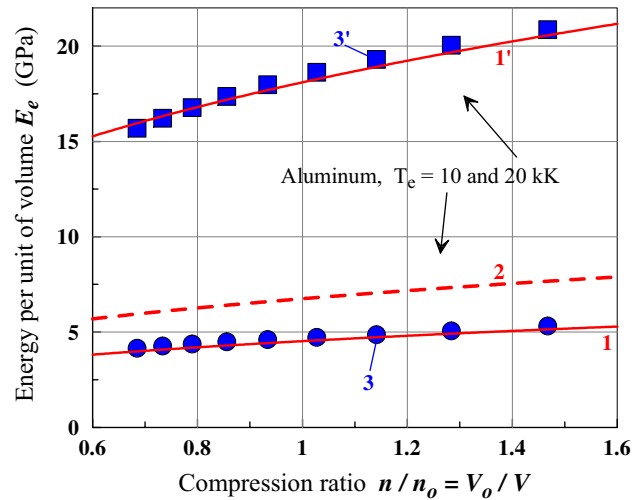

Fig. 6 Comparison of DFT data (the *filled circles* 3 and the *filled squares* 3') and the Fermi gas approach for aluminum. The *red curves* 1 and 1' correspond to the Fermi gas with $\gamma = 90.5 \text{ J/K}^2/\text{m}^3$. This is a theoretical value derived from expression (17) for $z = 3$ and m_e equal to the vacuum value. The *red dashed curve* 2 corresponds to the experimental low-temperature value $\gamma = 135 \text{ J/K}^2/\text{m}3$ [17, 18]. It is outside the DFT data range. This is similar to the results from [17] for electron heat capacity at the normal density Al, while here this is shown for the density range
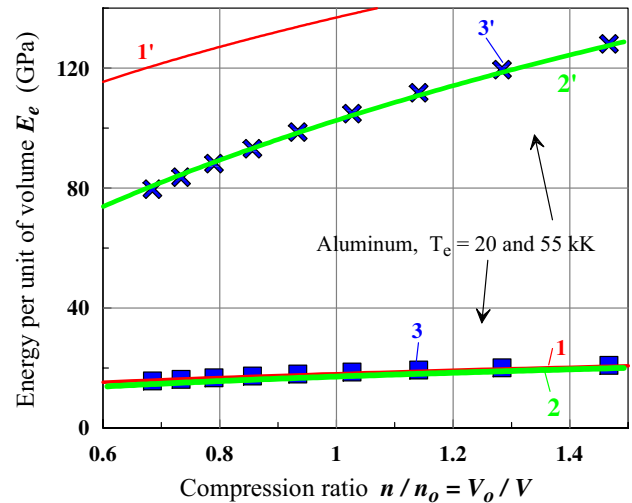

Fig. 7 Comparison of DFT data and its approximation for Al. The *red curves* 1 and 1' correspond to the Fermi gas model with $\gamma = 90.5 \text{ J/K}^2/\text{m}3$ for the two temperatures T_e equal to 20 and 55 kK, respectively. The *green curves* 2 and 2' present the combined approximation (18) for Al. The *filled squares* 3 and crosses 3' show DFT Elk data for $T_e = 20$ and 55 kK

Figures 6 and 7 present comparisons of our DFT data for aluminum obtained by the Elk package with the Fermi gas model and the combined approximation. The low-temperature dependencies of electron thermal energy are described well by the Fermi gas model. This conclusion is opposite to
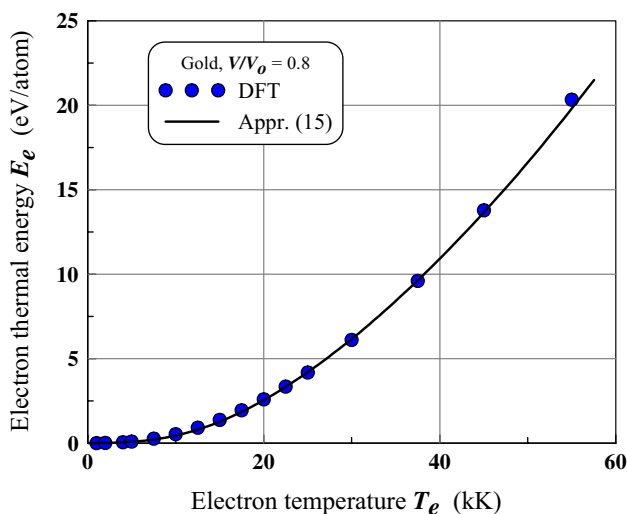
Fig. 8 Energy per atom from DFT data and its approximation (15) in the case of compressed gold
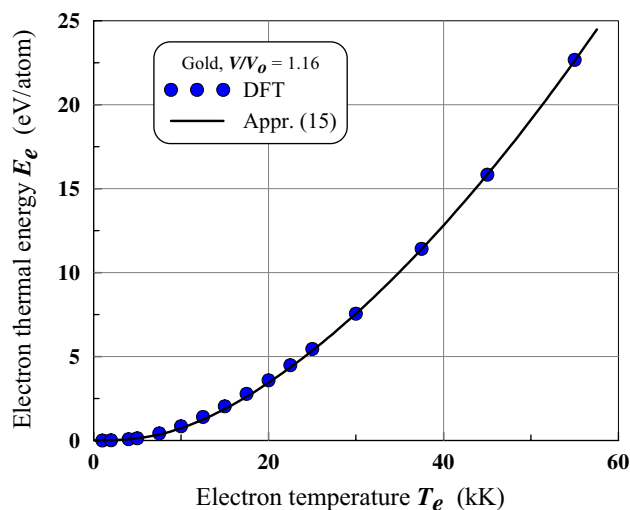

Fig. 9 Comparison of DFT data and its approximation (15) in the case of stretched gold

the conclusion obtained in the case of gold. The combined approximation shown in Fig. 7 describes energy very well in the wide ranges of temperatures and densities, while the Fermi model loses its validity at elevated temperatures T_e: compare curves 1' and 2' in Fig. 7. Our approximation shown as curves 2 and 2' in Fig. 7 combines the low- and high-temperature dependencies. It has a form

$$E_e(n, T_e) = \frac{C_{cl}}{\gamma} \left(\sqrt{C_{cl}^2 + \gamma^2 T_e^2} - C_{cl} \right), \tag{18}$$

where $C_{cl} = (3/2) z k_B n_o x$, $x = n/n_o$, γ is given by Eq. (17). To plot the curves 2 and 2' in Fig. 7, we have used the values $z = 3$ and m_e equal to the vacuum value. The electron heat capacity

$$c = 1/\sqrt{C_{cl}^{-2} + C_{deg}^{-2}}, \quad C_{deg} = \gamma T_e,$$

at a constant volume is given by the derivative of expression (18). Those expressions have been used in our previous 2T hydrodynamic simulations [4, 21–24] of laser–matter interaction in the case of aluminum.

In Figs. 8 and 9, the temperature dependencies of electron thermal energy per unit of mass are shown. They correspond to the densities near the edges of our range of compression/rarefaction ratios.

6 Comparison with DFT data for pressure and Gruneisen parameter

Figures 10 and 11 presents results of DFT calculations marked by 3 and 3', the approximation curves 2 and 2' (16), and the single-band Fermi gas function $p_e = (1/3)\gamma T_e^2$
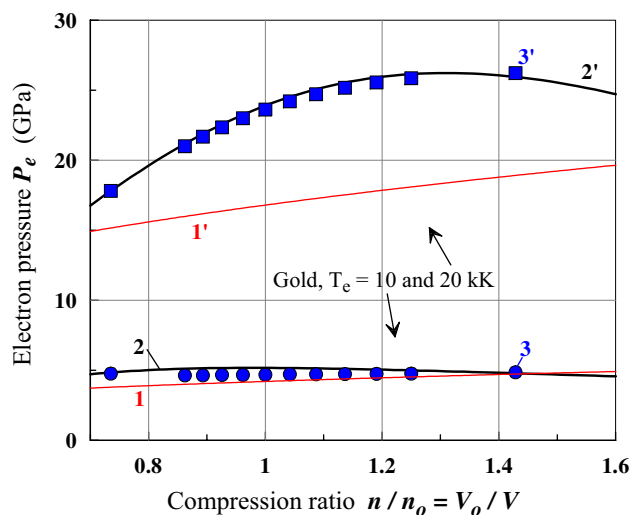

Fig. 10 Density dependence of electronic contribution to pressure. The Fermi theory results are shown by the *red curves* 1 and 1'; approximation (16)—the *black curves* 2 and 2'; and DFT data—the *filled circles* 3 and the *filled squares* 3'. They correspond to temperatures $T_e = 10$ kK (the bottom family) and $T_e = 20$ kK (the upper family)

marked by 1 and 1' Results cover a range of temperatures from rather small $T_e = 10$ and 20 kK to the high temperature $T_e = 55$ kK.

It is clear from Figs. 10 and 11 that the Fermi gas theory is valid up to temperatures ≈ 10 kK. But even at $T_e = 10$ kK the positive slope of the Fermi density (which is a power function with exponent 1/3) does not correspond to the DFT results; the function $p_e(n, T_e = 10 \, (kK))$ from our DFT calculations practically does not depend on density in the range of densities shown in Fig. 10. The Fermi
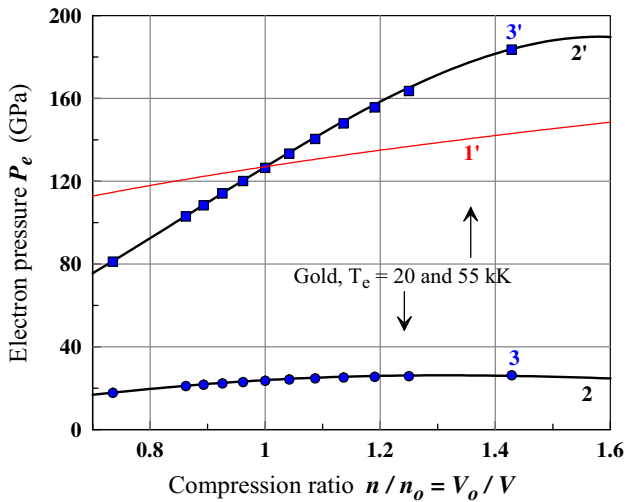
Fig. 11 Electron pressures in gold as functions of density at high temperatures T_e. The notations are identical to those in Fig. 10

Fig. 12 Variation of the Gruneisen parameter of gold with density and temperature T_e. *Markers* A, B, C and a, b, c correspond to the temperatures $T_e = 10, 20$ and 55 kK, respectively. A, B, C present DFT, while *curves* a, b, c show behavior in accordance with approximation (16). Low-temperature DFT data for the parameter Γ are higher than the Fermi gas value 2/3

theory significantly underestimates the electron pressure at the temperature $T_e = 20$ kK. The power law monotonic growth of the Fermi gas pressure $p_e = (1/3)\gamma T_e^2 \propto n^{1/3}$ at the constant temperature $T_e = 20$ kK, charge z, and mass m_e disagrees with the DFT behavior of pressure, see Fig. 10. At the high temperature $T_e = 55$ kK the pressure p_e in Fig. 11 increases with compression ratio much steeper than for the ideal Fermi gas.

In the Fermi gas model, the electron Gruneisen parameter Γ equals to 2/3 in the whole range of temperatures T_e from the degenerate gas to the classical gas. Temperature behavior of the parameter Γ for gold is shown in Fig. 12. DFT results for aluminum are shown in Figs. 13, 14, and 15. In the case of aluminum the values of the Gruneisen parameter are much more "stable" in comparison with gold, compare Figs. 12, and 15. At the fixed density, the temperature variation range of the parameter Γ is 2–3 times more narrow in the case of Al. Values of Γ for Al are more close to the Fermi gas value equal to 2/3.

We see that the approximations for energy (15) and pressure (16) of highly excited gold have accuracy high enough in the range of densities and temperatures T_e realized in the short pulse laser applications. In aluminum, the combination from the Fermi gas model and classical gas limit (18) is also accurate enough.

7 Two-temperature equation of state for metals

We separate the thermal electron contribution, associated with electron excitations, from the energy and pressure in a cold solid, as it is done in the Mie-Gruneisen approximation of EoS [8, 10, 28, 29]. Energy and pressure of the 2T EoS
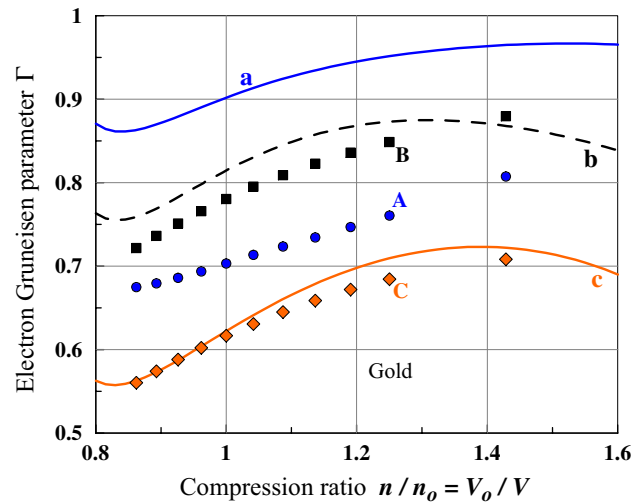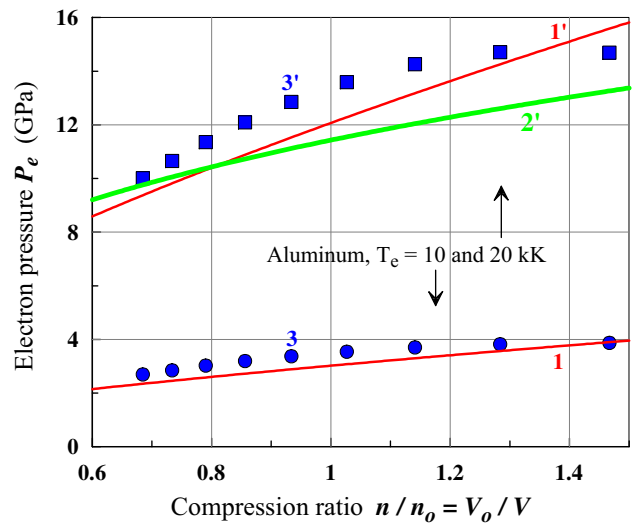

Fig. 13 Density dependence of electron pressure for aluminum. DFT data are shown by the *filled circles* 3 ($T_e = 10$ kK) and the *filled squares* 3' ($T_e = 20$ kK). The *red curves* 1 and 1' present the Fermi gas approach $p_e = (1/3)\gamma T_e^2$, $\gamma = 90.5$ J/K^2/m^3. The *green curve* 2' corresponds to the Eq. (18) taken with the Gruneisen parameter of 2/3

are presented as the sums of the cold energy and pressure, ion and electron thermal contributions to the energy and pressure as in [8, 10, 28, 29], but here with the separated ion and electron temperatures [10], also see related references in [30],

$$F(V, T_i, T_e) = F_o(V, 0, 0) + F_i(V, T_i, T_e) + F_e(V, T_i, T_e),$$
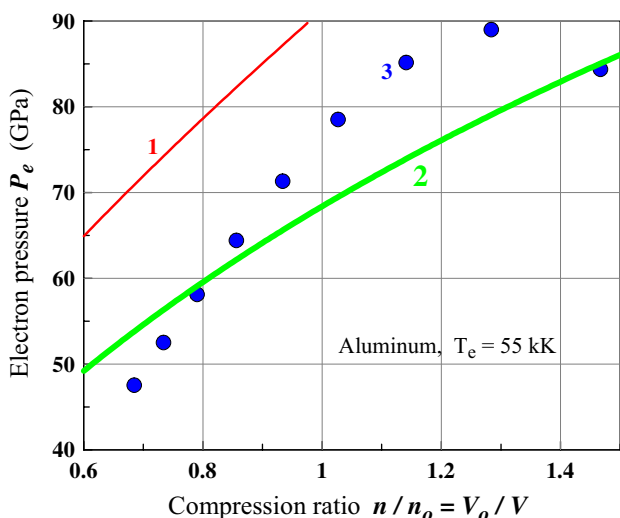
(19)

Fig. 14 Density dependence of electron pressure $p_e(n, T_e)$ for aluminum at the temperature $T_e = 55$ kK. The *red curve* 1 presents expression $p_e = (1/3)\gamma T_e^2$, the *green curve* 2 presents Eq. (18) taken with coefficient 2/3, and the *filled circles* 3 are DFT data
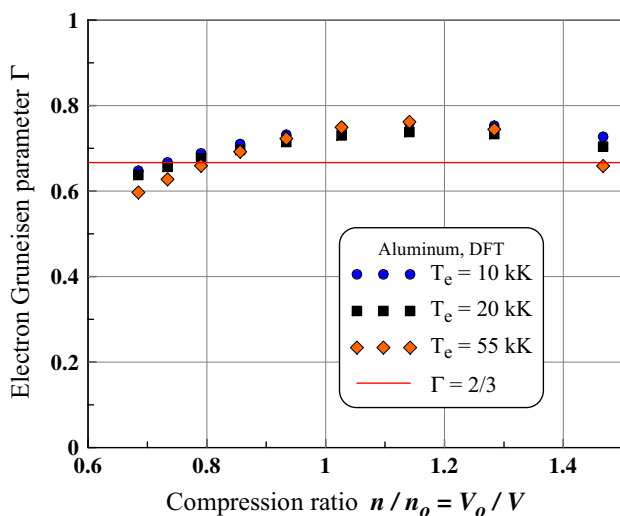

Fig. 15 Density dependence of the Gruneisen parameter for aluminum on the temperatures from DFT data

$$F(V, T_i, T_e) = F_o(V) + F_i(V, T_i, T_i) + F_e(V, T_e). \quad (20)$$

The ion part $F_o + F_i$ is taken from the wide-range EoS [8–10]. At the 2T state the electron free energy F_e (19, 20) gives a main contribution to the thermal and momentum balances in a surface layer of irradiated target.

Our approach [10, 30, 31] is based on the two following assumptions (1) and (2).

(1.) Changes in electron free energy F_e with T_i in the range of temperatures T_i up to few kK are small in compari-
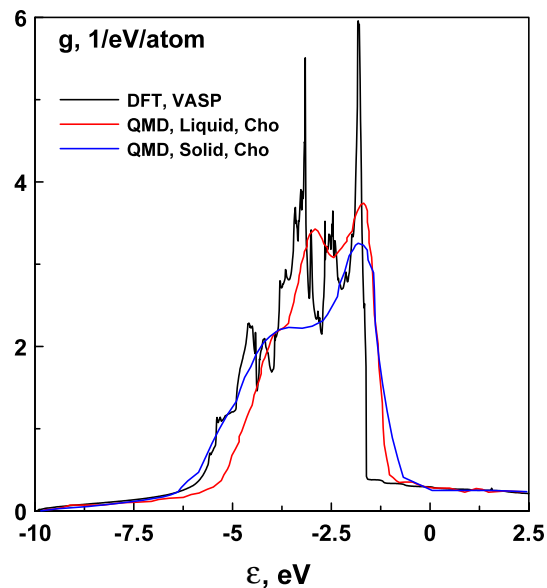

Fig. 16 DoS of Cu in liquid and solid state. The *black line* corresponds to VASP DFT calculation performed for cold solid Cu. The *blue line* and *red line* are taken from [32] for solid and liquid states, respectively

Fig. 17 The melting temperatures of seven metals obtained from the Lindemann criterion. The phonon spectra calculations are based on evaluations of elastic modules, used in the Lindemann criterion, similar to that done in [12]. The crosses are taken from [12]

son with changes of F_e caused by variation of electron temperatures in the range up to few eV (if mass density is fixed). This means that we neglect the variations of spectral features of an electron band structure caused by changes in the ion ordering if the density remains fixed. Figure 16 confirms that electron spectra are weakly sen-

sitive to an ion ordering. The correctness of assumption (1) is justified by the DFT calculations [32] of DoS for many different metals in solid and liquid states.

(2.) Variation of the electron temperature T_e affects rather weakly the ion free energy $F_o + F_i$ (19,20). Thus, the elastic modules of metal with hot electrons weakly depend on the electron temperature. Figure 17 demonstrates that the assumption (2.) is approximately valid only up to $T_e = 2$ eV with positive or negative changes of the melting temperatures with electron temperature. Those deviations depend on particular metal and are less than 15 % for $T_e < 2$ eV.

8 Conclusion

Series of DFT calculations of 2T gold and aluminum has been performed. DFT results cover a range of densities and electron temperatures, which are typical for the short pulse laser applications. For the first time, those DFT data are used to fit the several coefficients in the compact analytical approximations of 2T thermodynamics of metals, which were developed for using in 2T hydrodynamical codes. It is shown that the approximations of thermal energy and pressure describe well thermodynamics of gold in the 2T states, while the Fermi gas model is accurate for aluminum but it is not applicable for gold.

Appendix 1

In the case of Au, the Vienna ab-initio simulation package (VASP) [25, 26] was used in total energy and electron DoS calculations combined with the projected augmented wave (PAW) potential, the Perdew–Burke–Ernzerhof (PBE) exchange-correlation functional, and a kinetic energy cutoff of 500 eV. A $21 \times 21 \times 21$ Monkhorst-Pack k-point grid was used and electron occupation was treated with a Fermi–Dirac smearing method. The lattice constant for Au in equilibrium was found equal to 4.15 A. The number of empty states was set equal to 30. It is found that this value is enough for total energy calculations at high electron temperatures. Here we used the GGA-PBE approximation because it is more accurate for DoS calculation than LDA, but it gives the less accurate equilibrium lattice parameter (which was not aimed for improving in the present study).

For the Al total energy calculations, we use the FP-LAPW method implemented in the Elk code [27] and the PBE exchange-correlation functional. The muffin-tin radius of aluminum atoms of 2.20 a.u. is kept constant for all calculations; the number of k points is equal to $20 \times 20 \times 20$; and the product of the muffin-tin radius and the maximum reciprocal space vector is equal to 10. The maximum value for the waves inside the atomic spheres and the largest reciprocal vector in the charge Fourier expansion, Gmax, are set to 10 and 14, respectively. The self-consistent calculation is terminated when the total energy change is less than 10^{-6} eV in the case of VASP calculations for Au and less than 10^{-6} Ha in the case of Elk calculations for Al. In the latter case the tolerance for total potential change was limited by the value 10^{-6} Ha.

Appendix 2

Let us denote as $\mu(T_e)$ the electron chemical potential at the temperature T_e. Then the electron concentration is

$$zn = \frac{\sqrt{2}}{\pi^2} \left(\frac{\sqrt{m_s}}{\hbar} \right)^3 \int \frac{\varepsilon^{1/2} \, d\varepsilon}{\exp[(\varepsilon - \mu)/(k_B T_e)] + 1}.$$

(z is the number of electrons per atom, and n is the concentration of atoms). Correspondingly internal energy per unit volume, measured from the band bottom, is

$$E = \frac{\sqrt{2}}{\pi^2} \left(\frac{\sqrt{m_s}}{\hbar} \right)^3 \int \frac{\varepsilon^{3/2} \, d\varepsilon}{\exp[(\varepsilon - \mu)/(k_B T_e)] + 1}.$$

Values zn and E both are Fermi integrals

$$I(\mu) = \int \frac{F(\varepsilon) \, d\varepsilon}{\exp[(\varepsilon - \mu)/(k_B T_e)] + 1}$$

with functions $F(\varepsilon)$ correspondingly equal to $F(\varepsilon) = \varepsilon^{1/2}$ and $F(\varepsilon) = \varepsilon^{3/2}$. These integrals in the low-temperature limit in the fourth order in T_e are [14]

$$I(\mu) = \int_0^\mu F(\varepsilon) \, d\varepsilon$$
$$+ \frac{\pi^2}{6} F'(\mu)(k_B T_e)^2 + \frac{7\pi^4}{360} F'''(\mu)(k_B T_e)^4$$

To derive expressions (9) and (11), first we will find the expression for the chemical potential. Let us introduce the notation

$$A = \frac{\sqrt{2}}{\pi^2} \left(\frac{\sqrt{m_s}}{\hbar} \right)^3.$$

Then for the electron concentration we have

$$\frac{zn}{A} = \frac{2}{3} \mu^{3/2} + \frac{\pi^2}{6} \cdot \frac{1}{2\mu^{1/2}} (k_B T_e)^2$$
$$+ \frac{7\pi^4}{360} \cdot \frac{3}{8\mu^{5/2}} (k_B T_e)^4.$$

From the other side at $T_e = 0$ the same electron concentration can be written as

$$zn = A \frac{2}{3} E_F^{3/2}.$$

Hence we get

$$\frac{2}{3} E_F^{3/2} = \frac{2}{3} \mu^{3/2} + \frac{\pi^2}{12} \mu^{-1/2} (k_B T_e)^2 + \frac{7\pi^4}{960} \mu^{-5/2} (k_B T_e)^4$$

or

$$1 = \left(\frac{\mu}{E_F}\right)^{3/2} + \frac{\pi^2}{8} \left(\frac{\mu}{E_F}\right)^{-1/2} \left(\frac{k_B T_e}{E_F}\right)^2 + \frac{7\pi^4}{640} \left(\frac{\mu}{E_F}\right)^{-5/2} \left(\frac{k_B T_e}{E_F}\right)^4.$$

When introducing the denotion $k_B T_e / E_F = \tau$, we need to find coefficients c in the expression

$$\frac{\mu}{E_F} = 1 + c_1 \tau + c_2 \tau^2 + c_3 \tau^3 + c_4 \tau^4.$$

It is obvious that the coefficients of odd degrees of τ are equal to zero, therefore

$$\frac{\mu}{E_F} = 1 + c_2 \tau^2 + c_4 \tau^4.$$

With the accuracy including the term τ^4 we have

$$1 = 1 + \frac{3}{2} c_2 \tau^2 + \frac{3}{2} c_4 \tau^4 + \frac{3}{8} c_2^2 \tau^4 + \frac{\pi^2}{8} \left(1 - \frac{1}{2} c_2 \tau^2\right) \tau^2 + \frac{7\pi^4}{640} \tau^4$$

or

$$\left(\frac{3}{2} c_2 + \frac{\pi^2}{8}\right) \tau^2 + \left(\frac{3}{2} c_4 + \frac{3}{8} c_2^2 - \frac{\pi^2}{16} c_2 + \frac{7\pi^4}{640}\right) \tau^4 = 0.$$

Hence we find

$$c_2 = -\frac{\pi^2}{12}, c_4 = -\frac{\pi^4}{80}.$$

Now the asymptotic representation of the internal energy can be obtained. For the internal energy per atom E we have

$$\frac{En}{A} = \frac{2}{5} \mu^{5/2} + \frac{\pi^2}{6} \cdot \frac{3\mu^{1/2}}{2} (k_B T_e)^2 - \frac{7\pi^4}{360} \cdot \frac{3}{8\mu^{3/2}} (k_B T_e)^4.$$

Dividing this expression by the value $2E_F^{5/2}/5$ we obtain

$$\frac{En}{A} \frac{5}{2E_F^{5/2}} = \left(\frac{\mu}{E_F}\right)^{5/2} + \frac{5\pi^2}{8} \left(\frac{\mu}{E_F}\right)^{1/2} \tau^2 - \frac{7\pi^4}{384} \left(\frac{\mu}{E_F}\right)^{-3/2} \tau^4.$$

Substituting to this expression the expansion $\mu/E_F = 1 + c_2 \tau^2 + c_4 \tau^4$ and taking into account that

$$E_0 = \frac{1}{n} A \frac{2}{5} E_F^{5/2} = \frac{3}{5} z E_F$$

is the internal energy per atom at $T_e = 0$, we have with the accuracy up to terms τ^4

$$\frac{E}{E_0} = 1 + \frac{5}{2} c_2 \tau^2 + \frac{5}{2} c_4 \tau^4 + \frac{15}{8} c_2^2 \tau^4 + \frac{5\pi^2}{8} \left(1 + \frac{1}{2} c_2 \tau^2\right) \tau^2 - \frac{7\pi^4}{384} \tau^4$$

$$= 1 + \left(\frac{5}{2} c_2 + \frac{5\pi^2}{8}\right) \tau^2 + \left(\frac{5}{2} c_4 + \frac{15}{8} c_2^2 + \frac{5\pi^2}{16} c_2 - \frac{7\pi^4}{384}\right) \tau^4$$

Substituting here the above found coefficients c_2 and c_4, we obtain

$$E = E_0 \left(1 + \frac{5\pi^2}{12} \tau^2 - \frac{\pi^4}{16} \tau^4\right)$$

Then for thermal energy per atom we obtain

$$E_T = z E_F \left(\frac{\pi^2}{4} \tau^2 - \frac{3\pi^4}{80} \tau^4\right)$$

Now the entropy can be found:

$$s = \int_0^{T_e} \frac{dE_T}{T}$$

$$= z E_F \int_0^{T_e} \left(\frac{\pi^2}{4} \cdot \frac{k_B^2}{E_F^2} \cdot 2 - \frac{3\pi^4}{80} \cdot \frac{k_B^4}{E_F^4} \cdot 4T^2\right) dT$$

$$= z k_B \left(\frac{\pi^2}{2} \tau - \frac{\pi^4}{20} \tau^3\right)$$

The adiabatic condition $s = \text{const}$ therefore means $\tau = \text{const}$, and the thermal pressure can be written as

$$p_T = -\frac{\partial E_T}{\partial v}\Big|_s = -z \frac{dE_F}{dv} \left(\frac{\pi^2}{4} \tau^2 - \frac{3\pi^4}{80} \tau^4\right)$$

$$= \frac{2}{3} z n E_F \left(\frac{\pi^2}{4} \tau^2 - \frac{3\pi^4}{80} \tau^4\right).$$

References

1. M.B. Agranat, N.E. Andreev, S.I. Ashitkov, M.E. Veysman, P.R. Levashov, A.V. Ovchinnikov, D.S. Sitnikov, V.E. Fortov, K.V. Khishchenko, JETP Lett. **85**, 271–276 (2007)
2. J.P. Colombier, P. Combis, E. Audouard, R. Stoian, Phys. Rev. E **77**, 036409 (2008)
3. M.E. Povarnitsyn, T.E. Itina, K.V. Khishchenko, P.R. Levashov, Phys. Rev. Lett. **103**, 195002 (2009)
4. N.A. Inogamov, V.V. Zhakhovskii, S.I. Ashitkov, V.A. Khokhlov, V.V. Shepelev, P.S. Komarov, A.V. Ovchinnikov, D.S. Sitnikov, YuV Petrov, M.B. Agranat, S.I. Anisimov, V.E. Fortov, Contrib. Plasma Phys. **51**(4), 367–374 (2011)
5. P.A. Loboda, N.A. Smirnov, A.A. Shadrin, N.G. Karlykhanov, High Energy Density Phys. **7**, 361–370 (2011)
6. S. Anisimov, B. Kapeliovich, T. Perel'man, Sov. Phys. JETP **39**, 375–377 (1974)
7. D. Fisher, M. Fraenkel, Z. Henis, E. Moshe, S. Eliezer, Phys. Rev. E **65**, 016409 (2001)
8. A.V. Bushman, G.I. Kanel', A.L. Ni, V.E. Fortov, *Intense Dynamic Loading of Condensed Matter* (Taylor & Francis, London, 1993)
9. http://teos.ficp.ac.ru/rusbank/
10. N.A. Inogamov, YuV Petrov, V.V. Zhakhovsky, V.A. Khokhlov, B.J. Demaske, S.I. Ashitkov, K.V. Khishchenko, K.P. Migdal, M.B. Agranat, S.I. Anisimov, V.E. Fortov, I.I. Oleynik, in International Symposium on High Power Laser Ablation 2012. AIP Conference Proceedings **1464**, 593–608 (2012). doi:10.1063/1.4739912
11. K.P. Migdal, Yu.V. Petrov, and N.A. Inogamov, Fundamentals of laser-assisted micro- and nanotechnologies 2013, ed. by V.P. Veiko, T.A. Vartanyan, Proceedings of SPIE, Vol. 9065, 906503, (2013). doi:10.1117/12.2053172
12. V. Recoules, J. Clerouin, G. Zerah, P.M. Anglade, S. Mazevet, Phys. Rev. Lett. **96**, 055503 (2006)
13. E. Bevillon, J.P. Colombier, V. Recoules, R. Stoian, Phys. Rev. B **89**, 115117 (2014)
14. L.D. Landau, E.M. Lifshitz, *Statistical Physics* (Pergamon Press, Oxford, 1980)
15. S. Khakshouri, D. Alfe, D.M. Duffy, Phys. Rev. B **78**, 224304 (2008)
16. G.V. Sinko, N.A. Smirnov, A.A. Ovechkin, P.R. Levashov, K.V. Khishchenko, High Energy Density Phys. **9**, 309–314 (2013)
17. Zh Lin, L.V. Zhigilei, V. Celli, Phys. Rev. B **77**, 075133 (2008)
18. American Institute of Physics Handbook, 3rd edn. (McGraw-Hill, New York, 1972)
19. D.K. Ilnitsky, V.A. Khokhlov, N.A. Inogamov, V.V. Zhakhovsky, YuV Petrov, K.V. Khishchenko, K.P. Migdal, S.I. Anisimov, J. Phys. Conf. Ser. **500**, 032021 (2014)
20. N.A. Inogamov, V.V. Zhakhovsky, V.A. Khokhlov, B.J. Demaske, K.V. Khishchenko, I.I. Oleynik, J. Phys. Conf. Ser. **500**, 192023 (2014)
21. N.A. Inogamov, V.V. Zhakhovskii, S.I. Ashitkov, V.A. Khokhlov, Y.V. Petrov, P.S. Komarov, M.B. Agranat, S.I. Anisimov, K. Nishihara, Appl. Surf. Sci. **255**(24), 9712–9716 (2009). arXiv:0812.2965
22. V.V. Zhakhovskii, N.A. Inogamov, YuV Petrov, S.I. Ashitkov, K. Nishihara, Appl. Surf. Sci. **255**(24), 9592–9596 (2009)
23. M.B. Agranat, S.I. Anisimov, S.I. Ashitkov, V.V. Zhakhovskii, N.A. Inogamov, P.S. Komarov, A.V. Ovchinnikov, V.E. Fortov, V.A. Khokhlov, V.V. Shepelev, JETP Lett. **91**(9), 471–477 (2010)
24. N.A. Inogamov, V.V. Zhakhovsky, V.A. Khokhlov, V.V. Shepelev, JETP Lett. **93**(4), 226–232 (2011)
25. G. Kresse, J. Furthmuller, Comput. Mater. Sci. **6**, 15–50 (1996)
26. G. Kresse, J. Furthmuller, Phys. Rev. B **54**, 11169 (1996)
27. http://elk.sourceforge.net
28. P.R. Levashov, K.V. Khishchenko, AIP Conf. Proc. **706**, 87–90 (2004)
29. S.B. Kormer, V.D. Urlin, A.I. Funtikov, Sov. Phys. JETP **15**(3), 477–488 (1962)
30. YuV Petrov, N.A. Inogamov, JETP Lett. **98**(5), 278–284 (2013)
31. N.A. Inogamov, V.V. Zhakhovsky et al., Contrib. Plasma Phys. **53**(10), 796–810 (2013)
32. B.I. Cho, K. Engelhorn, A.A. Correa et al., Phys. Rev. Lett. **106**, 167601 (2011)